# Effect of mass transfer and kinetics in ordered Cu-mesostructures for electrochemical $CO_2$ reduction

Hakhyeon Song[a,1], Mintaek Im[b,1], Jun Tae Song[a,c], Jung-Ae Lim[b], Beom-Sik Kim[b,d], Youngkook Kwon[b,d,*], Sangwoo Ryu[a,e,**], Jihun Oh[a,c,f,**]

[a] Graduate School of Energy, Environment, Water, and Sustainability (EEWS), Korea Advanced Institute of Science and Technology (KAIST), Daejeon 34141, Republic of Korea
[b] Carbon Resources Institute, Korea Research Institute of Chemical Technology, Daejeon 34114, Republic of Korea
[c] KAIST Institute for NanoCentury, Korea Advanced Institute of Science and Technology (KAIST), Daejeon 34141, Republic of Korea
[d] Advanced Materials and Chemical Engineering, University of Science & Technology, Daejeon 34113, Republic of Korea
[e] Department of Advanced Materials Engineering, Kyonggi University, Suwon, Gyeonggi-do 16227, Republic of Korea
[f] Department of Materials Science and Engineering, Korea Advanced Institute of Science and Technology (KAIST), Daejeon 34141, Republic of Korea

## ARTICLE INFO

## ABSTRACT

Mass transfer, kinetics, and mechanism of electrochemical $CO_2$ reduction have been explored on a model mesostructure of highly-ordered copper inverse opal (Cu-IO), which was fabricated by Cu electrodeposition in a hexagonally-closed packed polystyrene template. As the number of Cu-IO layers increases, the formation of $C_2$ products such as $C_2H_4$ and $C_2H_5OH$ was significantly enhanced at reduced overpotentials (~200 mV) compared to a planar Cu electrode. At the thickest layer, we observe for the first time the formation of acetylene ($C_2H_2$), which can be generated through a kinetically slow reaction pathway and be a key descriptor in the unveiling of the C–C coupling reaction mechanism. Based on our experimental observation, a plausible reaction pathway in Cu mesostructures is rationalized.

## 1. Introduction

Electrochemical $CO_2$ reduction reaction ($CO_2RR$) using renewable energy sources can convert $CO_2$ into value-added hydrocarbon fuels and chemicals [1–9]. In particular, unsaturated $C_2$ hydrocarbons such as ethylene ($C_2H_4$) are promising feedstock for the synthesis of long-chain hydrocarbon and oxygenated fuels with a high volumetric energy density [10–12]. Cu is a unique metal that can produce hydrocarbons and alcohols with acceptable amounts from $CO_2RR$. The major $CO_2$ reduction products on the Cu catalyst range from $C_1$ compounds (e.g., CO, $HCOO^-$, and $CH_4$) to $C_2$ compounds (e.g., $C_2H_4$, $C_2H_5OH$, etc.). This is in sharp contrast to other metals that produce mostly one major $C_1$ (CO or $HCOO^-$) product [13–15]. This special ability of Cu offers chances to accelerate the C–C coupling toward the desired reaction products by designing a novel catalyst structure.

Many approaches have been demonstrated to tune and promote the Cu's ability to produce C–C coupled hydrocarbons and oxygenates by controlling the active sites of Cu (e.g., surface crystal facet [16,17],

grain boundary [18], and oxygen content [19–21]) as well as local electrolysis environments (e.g., electric field [22], electrolytes [23], and local pH evolution [24,25]). In particular, the meso- and nano-structuring of Cu catalysts has been successful in the highly selective $C_2$ product formation by regulating the interactions of reaction intermediates and $H^+$ and $OH^-$ at/near the Cu/electrolyte interface [26,27]. Ma et al. reported that the enhanced $C_2$ product formation on Cu nanowires (NWs) is attributed to the induced high local pH by increasing the length and density of the Cu NWs [26]. In addition, the temporal trapping of key intermediates in Cu meso-structures can facilitate C–C coupling, as demonstrated by porous Cu nanofoams (NFs) [28] and Cu mesostructures [29]. Dutta et al. reported that thick Cu NFs generate $C_2$ products ($C_2H_4$ and $C_2H_6$) with a Faradaic efficiency (FE) of 55% while the $C_1$ reaction path is suppressed due to the increased retention time of intermediates in mesoporous Cu catalysts [28]. However, the Cu mesostructures reported so far are non-uniform in size and length in the structures. Thus, the detailed role of the mesostructure toward mass transfer, kinetics, and reaction mechanisms for tunable

---

product selectivity remains unclear. Recently, Surendranath et al. reported that highly ordered nanoporous Au and Ag inverse opal (IO) structures can enable the systematic control of local pH in the IO structures, resulting in an increased selectivity of CO by tuning the IO thickness [30,31]. However, the $CO_2RR$ catalytic activity of IO mesostructures involved in the multi-electron/proton transfers for tunable $C_1$ and $C_2$ products has never been reported.

Herein, we demonstrate electrocatalytic $CO_2$ reduction on highly ordered mesoporous Cu-IO structures with controlled IO thicknesses. Our Cu-IO mesostructures exhibit a significantly enhanced $CO_2RR$ performance due to the increased surface area and can generate various $C_1$ (such as CO and $HCOO^-$) and $C_2$ (such as $C_2H_4$, and $C_2H_5OH$) products at low overpotentials. Increasing the Cu-IO thickness suppresses the formation of $CH_4$, which leads to the selective formation of $C_2H_4$ from the enhanced C−C coupling owing to the increased local pH and the prolonged retention time of intermediates in Cu-IO. Additionally, we observe, for the first time, the evolution of acetylene ($C_2H_2$) as a minor product in the thicker layers of Cu-IO. This study provides a platform to control the selectivity of $C_1$ and $C_2$ products by systematically controlling local environments during $CO_2RR$ and offers an insight in understanding the reaction mechanisms on Cu surfaces.

## 2. Experimental section

### 2.1. Fabrication of the Cu inverse opal structures

A hexagonally closed packed polystyrene (PS) template was synthesized by electrophoretic deposition (EPD). Sulfate-functionalized PS beads (ThermoFisher Scientific) of 600 nm in diameter were dispersed in ethanol and $NH_4OH$ was added to adjust the pH to over 10. The working electrode and the counter electrode for EPD are an electron-beam-evaporated Au (200 nm)/Ti (20 nm)/Si substrate and a Pt (35 nm)/Si substrate, respectively. The distance between the working and the counter electrodes was fixed at 1 cm, and 5 V was applied for six minutes to pile up PS beads over 15 layers. Subsequently, the template was annealed at 95 °C for 1 h to enhance the adhesion to the Au surface. Next, Cu was electrochemically deposited using a commercial acidic Cu-plating solution containing Cu sulfates. A constant current density of  − 10 mA cm$^{-2}$ was applied for 3, 6, and 12 minutes to fabricate IO structures with 3, 6, and 12 thickness layers. After the electroplating finished, samples were soaked into toluene for one day to remove the PS template.

### 2.2. Electrochemical analysis of products

#### 2.2.1. Electrochemical cells

Electrochemical H-type cells for $CO_2RR$ were designed to yield a high ratio of electrode surface to the electrolyte volume and analyzing gaseous products through an online gas chromatography. The details of the H-type cell were introduced in the previous research [32]. In brief, the cell is composed of anode and cathode chambers and separated by a Selemion AMV membrane (Asahi Glass Co.). Each chamber has a surface area of 1 cm$^2$ for working or counter electrodes, and a volume of 1.5 cm$^3$ for each electrolyte. A 1 mm OD Ag/AgCl reference electrode (Innovative Instruments, Inc., leak free series) and a glass gas frit bubbler were inserted into the cathode chamber to monitor the potential applied to the working electrode and to sparge $CO_2$ bubbles into the catholyte, respectively. The obtained potential was calibrated against a reversible hydrogen electrode. During the electrolysis, the catholyte was sparged with $CO_2$ (99.999%) and gaseous products were carried by $CO_2$ and directly injected into a gas chromatograph.

#### 2.2.2. Electrochemical conditions

In order to gain a high purity electrolyte, potassium carbonate ($K_2CO_3$, 99.995% trace metal basis, Sigma-Aldrich) was used as a precursor for making a 0.1 M bicarbonate electrolyte solution. Each

carbonate solution was sparged with 1 atm of $CO_2$ to be converted into a bicarbonate electrolyte until the pH of the $CO_2$-purged electrolyte became 6.8. Deionized water from a Millipore water purifying system that has a resistivity of 18.2 MΩ cm was used in this experiment. 3, 6, and 12 layered Cu-IOs on Au/Ti/Si substrates and Cu foil (0.1 mm thick, 99.9999%, Alfa-Aesar) were used as the working electrode. A Pt foil (0.1 mm thick, 99.99%, Alfa-Aesar) was cut into 2 × 2 cm and used as the counter electrode. Prior to each electrolysis, 1.5 mL of the electrolyte was injected into each chamber, and $CO_2$ was sparged through the cathode and anode chambers for 15 min. During electrolysis, $CO_2$ was constantly bubbled through the electrolyte at a flow rate of 5 sccm to prevent depletion of $CO_2$ even at high conversion rate and to ensure a constant flow of gas through the gas chromatograph.

Electrochemical analysis was performed using a Biologic SP-300 potentiostat. Potentiostatic electrochemical impedance spectroscopy (PEIS) was used to determine the total uncompensated resistance (Ru) by applying frequencies from 5 Hz to 1 MHz at the open circuit potential. The potentiostat compensated for 85% of Ru *in situ*, and the last 15% was postcorrected to arrive at accurate potentials. After linear sweep voltammetry (LSV) at a scan rate of 20 mV s$^{-1}$ from  − 0.3 V to  − 1.8 V vs. Ag/AgCl, a static voltage was applied for one hour using the chronoamperometry method. The product distribution analyzed by gas chromatography (GC) and high-performance liquid chromatography (HPLC) was converted into Faradaic efficiency for each product. Potentials were converted into the reversible hydrogen electrode (RHE) scale (all potentials here are referred to this reference) as follows:

$$E(vs. RHE) = E(vs. Ag/AgCl) + 0.197 V + 0.0591 \times pH$$

#### 2.2.3. Product analysis

Gaseous products generated at the cathode were delivered into an online gas chromatograph (iGC 7200, DS science) for the analysis. The $CO_2$ flow rate was set to 5 sccm, which was controlled with a mass flow controller (BROOKS Instrument, 5850E series). Gaseous products such as $H_2$, CO, $CH_4$, $C_2H_2$, $C_2H_4$, and $C_2H_6$ were separated in a carbon column (Carboxen® 1006 PLOT, SUPELCO) and detected by a helium ionization detector (HID) (Valco Instrument Co, Inc.). The calibration of the gas chromatograph was carried out using a standard gas mixture (1000 ppm of expected products, Rigas). Gaseous products were analyzed every 13 minutes during the electrolysis and all of the values were averaged.

Liquid products were collected from the cathode and anode chambers after electrolysis. They were also analyzed by HPLC (1260 Infinity II, Agilent Technologies) with a SUGAR SH1101 column (Shodex). 1 mM sulfuric acid was used as an eluent, and 50 μL of the sample was automatically injected into the column using an autosampler. The column was maintained at 75 °C in a column oven, and a refractive index detector (RID) was used to detect the separated products. A standard calibration curve of the expected products was drawn in the same condition.

## 3. Results and discussion

### 3.1. Characterization of Cu inverse opals

Fig. 1a–e show the scanning electron microscopy (SEM, Magellan 400) and digital images of the Cu-IO and planar structures. A Cu-IO is an ordered 3-dimensional (3D) mesoporous structure with a controlled surface area and thickness (Fig. 1a–d). A Cu-IO was created by electroplating Cu into hexagonally-closed packed polystyrene (PS, diameter of 600 nm) templates, followed by the selective removal of the PS templates (see experimental section and supporting information 1 (S1)). Cu-IOs with 3, 6, and 12 layers were formed by controlling the Cu electroplating times (Fig. 1b–d). Hereafter, we denote Cu-IOs with different layers as the Cu-IO-layer thickness. The total thickness of
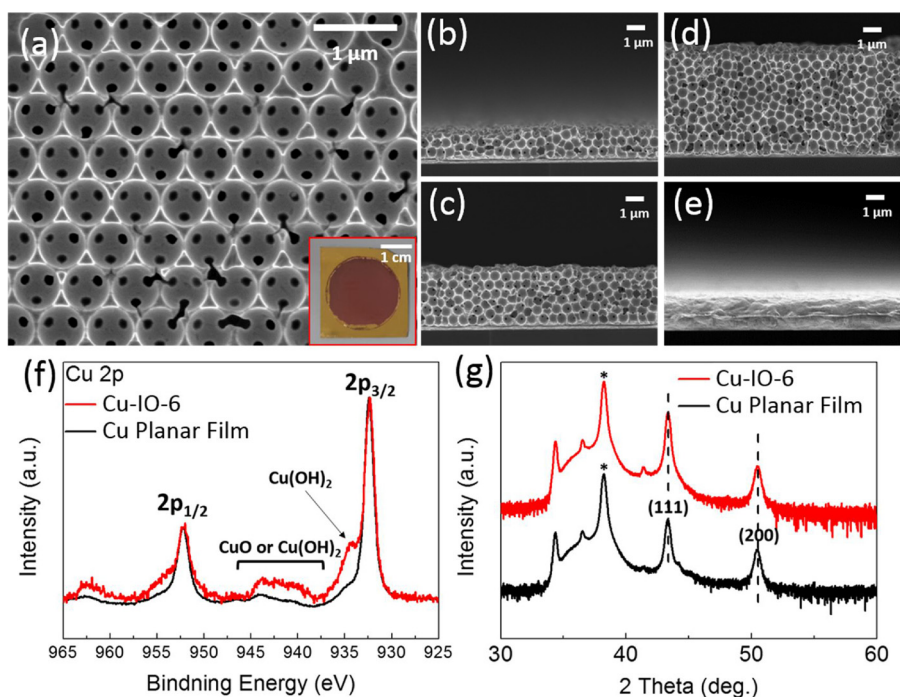
**Fig. 1.** (a) Top view cross-sectional scanning electron microscopy (SEM) image of a Cu inverse opal (Cu-IO) mesostructure with 6 layers (Cu-IO-6). The inset of a) is a digital photograph image of the electrodeposited Cu-IO-6; (b–e) cross-sectional SEM images of Cu-IO-3, Cu-IO-6, Cu-IO-12, and a Cu planar film, respectively. The Cu planar film is electroplated using the same condition used to form Cu-IO-6; (f) X-ray photoelectron spectroscopy (XPS) and (g) X-ray diffraction (XRD) patterns of the Cu planar film and Cu-IO-6. The * mark indicates a peak from the Au plating base used for electrodeposition.

mesoporous Cu-IOs is linearly proportional to the layer thickness and becomes ~6 μm for Cu-IO-12 (Fig. 1d).

A planar Cu film was also formed by the same electroplating condition (Fig. 1e). The Cu planar and IO electrodes used in this work are over 5 $cm^2$ in the geometric area. X-ray photoelectron spectroscopy (XPS, K-alpha Thermo VG scientific) reveals that the surface chemical states of both the Cu planar and IO films are mostly metallic Cu while Cu oxide and hydroxide peaks are also present (Fig. 1f) [33–35]. Notably, the Cu-IOs show a slightly high intensity of Cu oxide and hydroxide, which can be attributed to the high surface area of the Cu-IO. Fig. 1g shows X-ray diffraction (XRD, Ultima IV, Rigaku) patterns of the Cu planar and IO films. Only (111) and (200) diffraction peaks of both the Cu planar and IO films appear, indicating that the two electrodes have a similar crystal orientation [36]. Therefore, the catalytic activity of Cu-IO is anticipated to be directly influenced by mesostructures such as the thickness of layers rather than Cu oxidation states or crystallinity.

### 3.2. Electrochemical analysis of Cu inverse opals

Fig. 2a and b present the total and partial $CO_2RR$ current density-potential curves of Cu planar and IOs with various layer thicknesses in $CO_2$-saturated 0.1 M $KHCO_3$, respectively. The total current density shown in Fig. 2a includes the hydrogen evolution reaction (HER) and $CO_2RR$ while the $CO_2RR$ current density in Fig. 2b only includes $CO_2$ conversion. The detailed Faradaic efficiency of the reaction products is summarized in Table S1. As clearly shown in Fig. 2a and b, a high surface area of Cu-IO mesostructures significantly improves the electrocatalytic performance for both HER and $CO_2RR$ at low overpotentials. For instance, the Cu-IO-12 reaches a total current density of −62 mA $cm^{-2}$ at −0.81 V. Interestingly, the amount of $CO_2$ conversion saturates when the IO layer increases more than 6 layers. In addition, Tafel analysis reveals that the Tafel slope at high overpotentials gradually increases from ~155 to 340 mV $dec^{-1}$ with an increase in the Cu-IO layers, while the Cu planar and IOs show similar Tafel slopes (~358–411 mV $dec^{-1}$) at low overpotentials (Fig. S2). This indicates the impeded transportation of the reactants and products at an increased conversion rate of $CO_2$ in Cu-IO mesostructures, although the pH of the bulk electrolyte of Cu-IOs remained unchanged after electrolysis. It is also important to note that the mesostructure of Cu-IO is
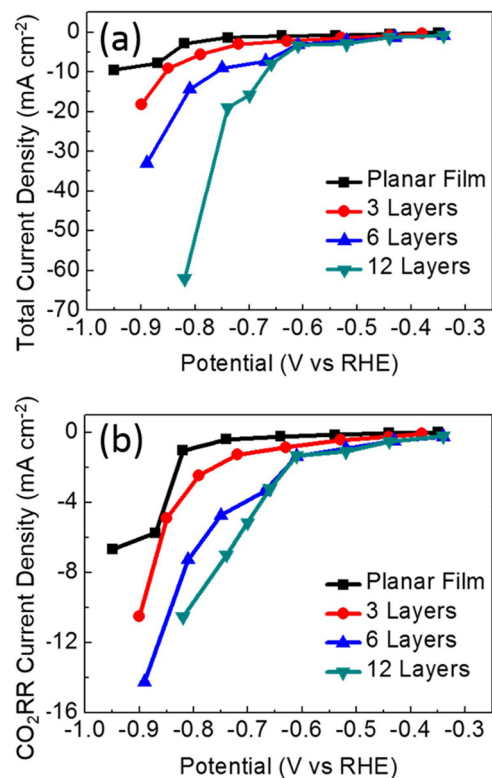




**Fig. 2.** (a) Total and (b) partial $CO_2$ reduction reaction ($CO_2RR$) current density of a Cu planar film and Cu-IOs with various thicknesses as a function of applied potential in $CO_2$-saturated 0.1 M $KHCO_3$.

maintained after one hour of electrolysis (Figs. S3, S4).

The modification of $CO_2RR$ kinetics in Cu-IO mesostructures yields a distinctively different potential-dependence of $CO_2RR$ product distribution compared to the Cu planar electrodes. Faradaic efficiencies (FE) of the reaction products on the Cu planar film and IOs with various layers are summarized in Fig. 3. Upon the suppression of $H_2$ evolution, Cu-IO mesostructures generate a large amount of $CO_2RR$ products at a
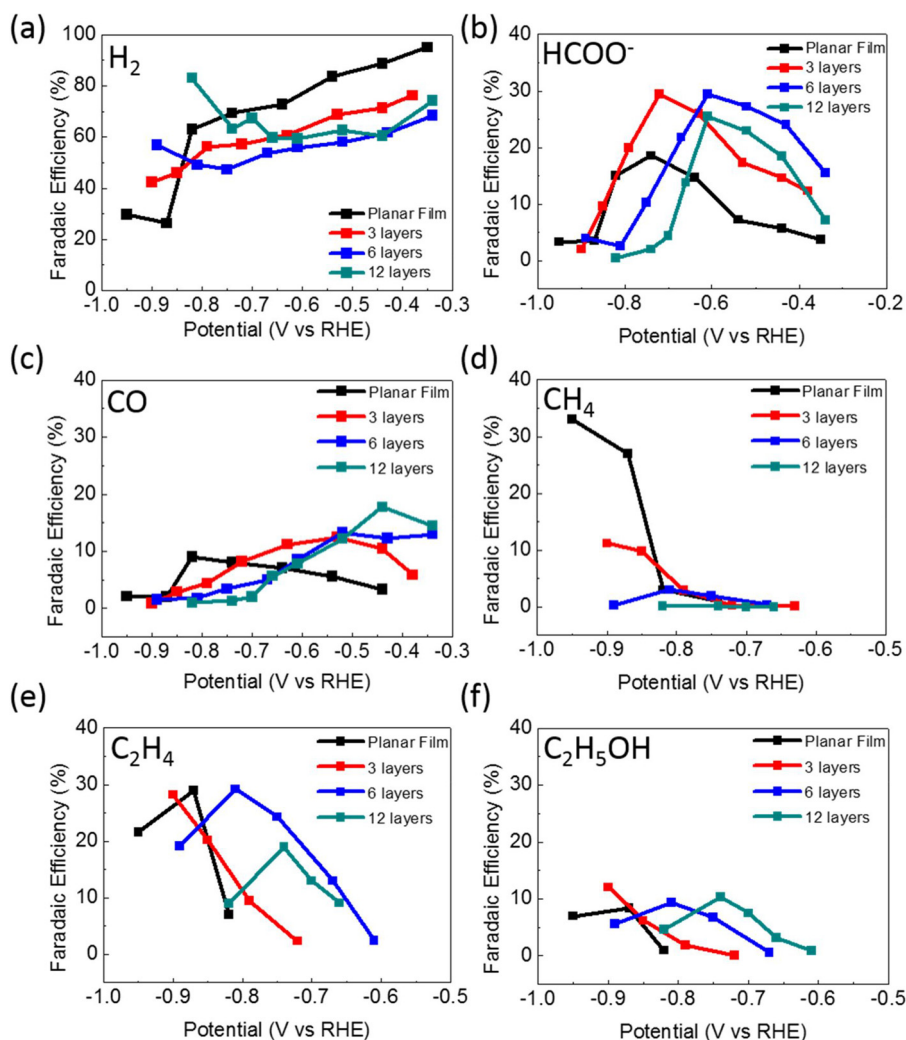
**Fig. 3.** Faradaic efficiency (FE) of (a) $H_2$, (b) $HCOO^-$, (c) CO, (d) $CH_4$, (e) $C_2H_4$ and (f) $C_2H_5OH$ on the Cu planar film and Cu-IOs as a function of applied potential in $CO_2$-saturated 0.1 M $KHCO_3$ electrolytes.

lower overpotential compared to the Cu planar electrode, except for $CH_4$. The reduced overpotential of Cu-IOs can be attributed to, in part, increased active sites from a high surface area of the mesostructures, and the significant decrease in FE of $H_2$ could originate from the increased alkalinity caused by the limited mass transfer of $CO_2RR$ by-products, i.e., $OH^-$ ions, at/near highly porous IO structures. Similar phenomena were observed from Au [22], Ag-IO [30,31], and Cu NWs [26] mesostructure electrodes. Note that the upturn of the FE of $H_2$ at a high overpotential for Cu-IO-6, and Cu-IO-12 in Fig. 3a may result from the limited available $CO_2$ and inevitable polarization losses [37]. With the suppression of HER, as shown in Fig. 3 b, Cu-IOs enhance the maximum FE of $HCOO^-$ to ~30% compared to ~20% of the Cu planar electrode. Moreover, the overpotential for the maximum FE of $HCOO^-$ decreases as Cu-IOs become thicker. Recent theoretical modeling suggests that $HCOO^-$ is formed by the reaction of the physisorbed $CO_2$ with surface $H_{ad}$ [38]. In addition, Sen et al. reported that the selectivity of $HCOO^-$ is affected by the roughness and porosity of Cu NFs [39]. Therefore, the enhanced selectivity of Cu-IO mesostructures for $HCOO^-$ formation is believed to originate from a high surface area and reduced HER to promote $CO_2$ adsorption and protonation in Cu-IOs.

The formation of $CH_4$, $C_2H_4$, and $C_2H_5OH$, which is strongly influenced by the Cu-IO mesostructures, shows a direct correlation with CO formation (Fig. 3c–f). Firstly, the thicker Cu mesostructures promote the formation of CO, which is the key intermediate for hydrocarbons and oxygenates, at a lower overpotential (Fig. 3c). In contrast, $CH_4$

production, which typically occurs at potential < −0.8 V [40,41], gradually decreases as the Cu-IO layers increase. As a result, the FE of $CH_4$ in Cu-IO-12 becomes less than 1% over all the potential ranges, as presented in Fig. 3d, and the ratio of $C_2H_4$ to $CH_4$ in Cu-IO-12 reaches ~95 at −0.74 V. As clearly shown in Fig. 3e and f, both Cu planar and IO mesostructures produce $C_2H_4$ and $C_2H_5OH$ with an FE of ~30 and 10%, respectively, but the Cu-IOs facilitate the formation of $C_2$ compounds at more positive potentials. Notably, in the Cu-IOs, the overall $C_2$ production rises following the decline of CO production and the negligible production of $CH_4$. This strongly suggests that the Cu mesostructures enhance C−C coupling by CO−CO(H) dimerization for selective $C_2$ products formation, which is consistent with the literature [26].

Interestingly, acetylene ($C_2H_2$, FE of ~3% at −0.61 V) and ethane ($C_2H_6$, FE of 2–3% at −0.66 V) were produced in the significant presence of CO and $C_2H_4$, but only in the thick IO structures (Cu-IO-12), as shown in Fig. 4. Here we identify, for the first time, the electrochemical conversion of $CO_2$ into $C_2H_2$. It is important to note that the onset potential of $C_2H_2$ formation (−0.61 V) is 50 mV positive compared with those of ethylene ($C_2H_4$) and ethane ($C_2H_6$). This indicates that $C_2$ hydrocarbons can be generated via $C_2H_2$ as a key intermediate, which has been only proposed in theoretical work [42]. It is reasonable that under a strong reduction environment, $C_2H_2$ rapidly disappears as the overpotential increases.
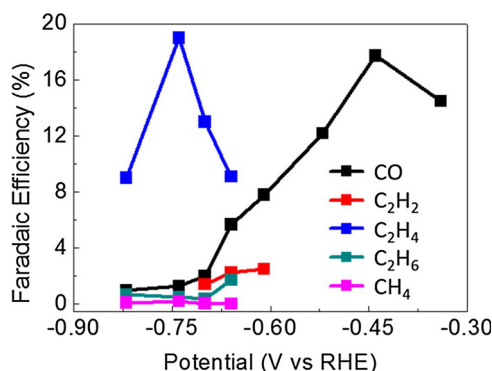
**Fig. 4.** The selectivity of gas product from Cu-IO-12 as a function of applied potential in $CO_2$-saturated 0.1 M $KHCO_3$ electrolytes.

### 3.3. CO₂ Reduction reaction pathway

To elucidate the potential-dependent selectivity of major and minor $CO_2RR$ products in Cu mesostructures, we propose reaction pathways of $CO_2$ reduction on the Cu surface in Scheme 1. The solid and dotted lines represent the reaction paths for major and minor products, respectively, in reference to the relative energy barriers from recent computational studies [38,41–44]. First of all, $HCOO^-$ is formed by the direct protonation of adsorbed $CO_2$ [38], and adsorbed CO ($CO_{ad}$) is generated through the adsorbed $COO^-$ intermediate [45] Then, $CO_{ad}$ can be further protonated to major products (e.g. $CH_4$ and $C_2H_4$) at low or high overpotential ranges with different mechanisms. It has been proposed that at high overpotentials, the production of $CH_4$ proceeds with a sequential protonation of $CH_{x,ad}$ derived from $COH_{ad}$ or $CHO_{ad}$ intermediates, and $C_2H_4$ forms through $CH_{x,ad}$ dimerization [43]. However, at a low overpotential region, $C_2H_4$ can be formed via CO-CO(H) dimerization, which requires about 280 mV lower overpotential than the dimerization from the intermediates ($COH_{ad}$ or $CHO_{ad}$) at a high overpotential [41]. In addition, it is known that CO−CO(H) dimerization favors a high local pH as the Koper and Mul groups reported [22,25,40]. Therefore, Cu-IO mesostructures promote the formation of $C_2H_4$ at a low overpotential by CO−CO(H) dimerization under a high local pH induced in the mesostructure. However, at high overpotentials,

the production of $CH_4$ is highly suppressed in Cu-IOs and $C_2H_4$ formation could be partially attributed to $CH_{2,ad}$ dimerization [43].

Cu-IOs also activate the reaction path for the minor products such as $C_2H_2$ and $C_2H_6$ by increasing the retention time of intermediates and reducing the available protons in the mesostructures. As shown in Fig. 4, $C_2H_2$ is observed only in Cu-IO-12. Recently, Xiao et al. predicted that the formation of $C_2H_2$ is ill-favored because of the fast electrochemical hydrogenation to $H_2C=CH_{ad}$ and the high non-electrochemical desorption energy of $HC=CH_{ad}$ [42]. Consequently, we suggest that the observation of $C_2H_2$ in Cu-IO-12 is probably driven by a slow protonation of $HC=C_{ad}$ (Scheme 1, dotted line) owing to the limited proton sources and by the facilitated desorption of $HC=CH_{ad}$ from an increased retention time in Cu-IO-12.

Indeed, the lack of proton sources in Cu-IO-12 can be correlated with the trend of HER. For instance, Cu-IO-6 and Cu-IO-12 show nearly identical HER partial current densities at – 0.6 V where the FE of $C_2H_2$ reaches the highest, although Cu-IO-12 has a two time greater surface area than Cu-IO-6 (Fig. S5). This implies that the hydrogen evolution per active sites in Cu-IO-12 is about half of that in Cu-IO-6. When HER increases at potential < −0.6 V, $C_2H_4$ formation dominates with a rapid decline of $C_2H_2$ (Fig. 4). Likewise, the formation of $C_2H_6$ is thought to occur due to the increased retention time of intermediates (e.g., $HC=CH_{ad}$, $H_2C=CH_{ad}$, $C_2H_2$, or $C_2H_4$) in Cu-IO-12, as illustrated in Scheme 1 [42].

### 3.4. Highly enhanced CO₂ reduction performance of Cu inverse opals

With a controlled local environment and high surface area, Cu-IOs show a high performance toward $C_2$ formation at a low overpotential. As shown in Fig. S6, Cu-IO-12 shows an overpotential reduction of ~180 mV compared to the Cu planar electrode at the $C_2$ partial current density of −2 mA cm$^{-2}$. Moreover, Cu-IO-12 exhibits a $C_2$ production current density of ~ −9 mA cm$^{-2}$ at −0.81 V, although Cu-IO-6 shows a higher $C_2$ selectivity. As benchmarked in Table S2, the $CO_2RR$ performance for the $C_2$ production ($C_2H_4$ and $C_2H_5OH$) of our Cu-IOs is superior or comparable to the state-of-the-art electrocatalysts.

### 4. Conclusions

In summary, we developed highly ordered 3D Cu-IO mesostructures
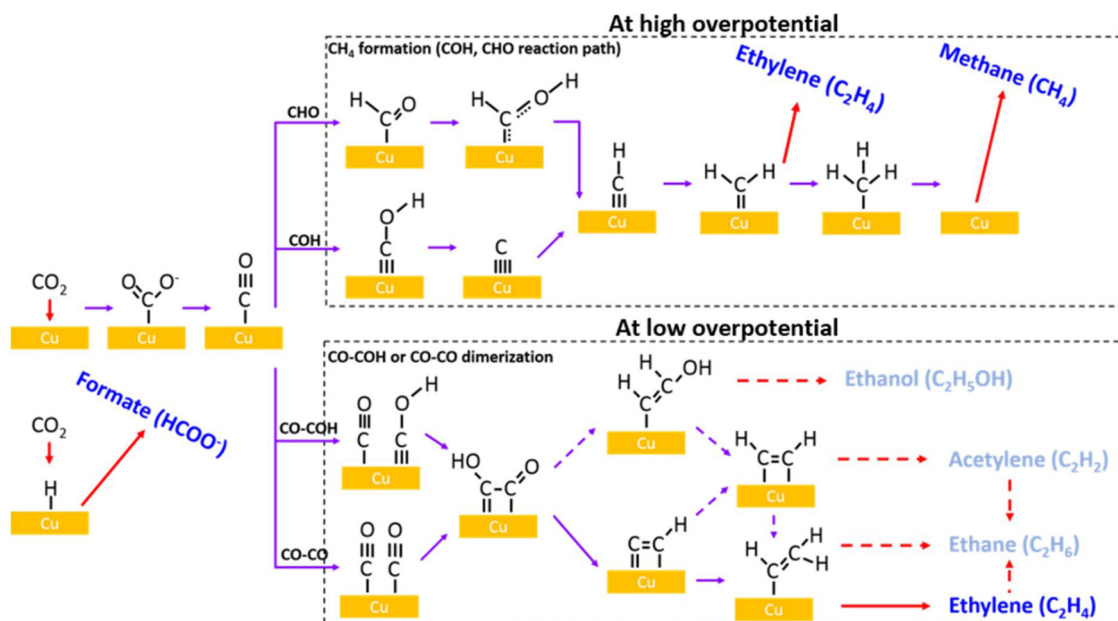


**Scheme 1.** Reaction paths proposed for the formation of formate, methane, and various $C_2$ products such as acetylene, ethylene, ethane, and ethanol during the electrochemical $CO_2RR$ on the Cu surface. Solid and dotted lines indicate the reaction paths for major and minor products, respectively.

with uniform and controlled meso-pores for high performance and selective $CO_2$ reduction electrocatalysts. With various layers of Cu-IOs, we systematically controlled the potential-dependent distribution of $C_1$ products (CO, $HCOO^-$) and $C_2$ products ($C_2H_4$, $C_2H_5OH$). From this study, we can identify that Cu mesostructures favor $C_2$ formation at a low overpotential by providing more active reaction sites, changing the local environment, and increasing the retention time of intermediates. Moreover, when these occur in the thickest Cu-IO, it allows a kinetically slow reaction pathway for the formation of $C_2H_2$, which is observed for the first time as the product of the electrochemical conversion of $CO_2$. This study provides insights on the importance of mesostructures in $CO_2RR$ to tune the product selectivity and understand the reaction mechanisms.

Supplementary data associated with this article can be found in the online version at doi:

## Acknowledgements

## Appendix A. Supplementary data

Supplementary material related to this article can be found, in the online version, at doi:https://doi.org/10.1016/j.apcatb.2018.03.071.

## References

[1] J.L. White, M.F. Baruch, J.E. Pander III, Y. Hu, I.C. Fortmeyer, J.E. Park, T. Zhang, K. Liao, J. Gu, Y. Yan, Chem. Rev. 115 (2015) 12888–12935.
[2] Z.W. Seh, J. Kibsgaard, C.F. Dickens, I. Chorkendorff, J.K. Nørskov, T.F. Jaramillo, Science 355 (2017) eaad4998.
[3] J.T. Song, H. Ryoo, M. Cho, J. Kim, J.G. Kim, S.Y. Chung, J. Oh, Adv. Energy Mater. 7 (2017).
[4] M. Cho, J.-W. Seo, J.T. Song, J.-Y. Lee, J. Oh, ACS Omega 2 (2017) 3441–3446.
[5] X. Jiang, N. Koizumi, X. Guo, C. Song, Appl. Catal. B Environ. 170 (2015) 173–185.
[6] J. Ding, Y. Bu, M. Ou, Y. Yu, Q. Zhong, M. Fan, Appl. Catal. B Environ. 202 (2017) 314–325.
[7] Z. Xiong, Z. Lei, C.-C. Kuang, X. Chen, B. Gong, Y. Zhao, J. Zhang, C. Zheng, J.C. Wu, Appl. Catal. B Environ. 202 (2017) 695–703.
[8] X. Dong, F. Li, N. Zhao, F. Xiao, J. Wang, Y. Tan, Appl. Catal. B Environ. 191 (2016) 8–17.
[9] Q. Shen, X. Huang, J. Liu, C. Guo, G. Zhao, Appl. Catal. B Environ. 201 (2017) 70–76.
[10] G. Kyriakou, J. Kim, M.S. Tikhov, N. Macleod, R.M. Lambert, J. Phys. Chem. B 109 (2005) 10952–10956.
[11] D.S. McGuinness, Chem. Rev. 111 (2011) 2321–2341.
[12] K.D. Yang, C.W. Lee, K. Jin, S.W. Im, K.T. Nam, J. Phys. Chem. Lett. 8 (2017) 538–545.
[13] Y.S. Ham, S. Choe, M.J. Kim, T. Lim, S.-K. Kim, J.J. Kim, Appl. Catal. B Environ. 208 (2017) 35–43.
[14] M.S. Jee, H.S. Jeon, C. Kim, H. Lee, J.H. Koh, J. Cho, B.K. Min, Y.J. Hwang, Appl. Catal. B Environ. 180 (2016) 372–378.
[15] J.-H. Kim, H. Woo, S.-W. Yun, H.-W. Jung, S. Back, Y. Jung, Y.-T. Kim, Appl. Catal. B Environ. 213 (2017) 211–215.
[16] C. Hahn, T. Hatsukade, Y.-G. Kim, A. Vailionis, J.H. Baricuatro, D.C. Higgins, S.A. Nitopi, M.P. Soriaga, T.F. Jaramillo, Proc. Natl. Acad. Sci. (2017) 201618935.
[17] W. Luo, X. Nie, M.J. Janik, A. Asthagiri, ACS Catal. 6 (2015) 219–229.
[18] X. Feng, K. Jiang, S. Fan, M.W. Kanan, ACS Cent. Sci. 2 (2016) 169–174.
[19] H. Mistry, A.S. Varela, C.S. Bonifacio, I. Zegkinoglou, I. Sinev, Y.-W. Choi, K. Kisslinger, E.A. Stach, J.C. Yang, P. Strasser, Nat. Commun. 7 (2016).
[20] D. Gao, F. Scholten, B. Roldan Cuenya, ACS Catal. (2017).
[21] D. Gao, I. Zegkinoglou, N.J. Divins, F. Scholten, I. Sinev, P. Grosse, B. Roldan Cuenya, ACS Nano 11 (2017) 4825–4831.
[22] J.H. Montoya, C. Shi, K. Chan, J.K. Nørskov, J. Phys. Chem. Lett. 6 (2015) 2032–2037.
[23] M.R. Singh, Y. Kwon, Y. Lum, J.W. Ager III, A.T. Bell, J. Am. Chem. Soc. 138 (2016) 13006–13012.
[24] Y. Hori, A. Murata, R. Takahashi, J. Chem. Soc. Faraday Trans. 85 (1989) 2309–2326.
[25] R. Kas, R. Kortlever, H. Yılmaz, M. Koper, G. Mul, ChemElectroChem 2 (2015) 354–358.
[26] M. Ma, K. Djanashvili, W.A. Smith, Angew. Chem. 128 (2016) 6792–6796.
[27] T.T. Hoang, S. Ma, J.I. Gold, P.J. Kenis, A.A. Gewirth, ACS Catal. 7 (2017) 3313–3321.
[28] A. Dutta, M. Rahaman, N.C. Luedi, M. Mohos, P. Broekmann, ACS Catal. 6 (2016) 3804–3814.
[29] K.D. Yang, W.R. Ko, J.H. Lee, S.J. Kim, H. Lee, M.H. Lee, K.T. Nam, Angew. Chem. Int. Ed. 56 (2017) 796–800.
[30] A.S. Hall, Y. Yoon, A. Wuttig, Y. Surendranath, J. Am. Chem. Soc. 137 (2015) 14834–14837.
[31] Y. Yoon, A.S. Hall, Y. Surendranath, Angew. Chem. 128 (2016) 15508–15512.
[32] P. Lobaccaro, M.R. Singh, E.L. Clark, Y. Kwon, A.T. Bell, J.W. Ager, Phys. Chem. Chem. Phys. 18 (2016) 26777–26785.
[33] C.D. Wagner, G. Muilenberg, Handbook of X-ray Photoelectron Spectroscopy, Perkin-Elmer Corp., 1979.
[34] T. Waechtler, S. Oswald, N. Roth, A. Jakob, H. Lang, R. Ecke, S.E. Schulz, T. Gessner, A. Moskvinova, S. Schulze, J. Electrochem. Soc. 156 (2009) H453–H459.
[35] C. Zhu, A. Osherov, M.J. Panzer, Electrochim. Acta 111 (2013) 771–778.
[36] W.-S. Su, M.-S. Tsai, W. Fang, Electrochem. Solid State Lett. 10 (2007) H16–H19.
[37] M.R. Singh, E.L. Clark, A.T. Bell, Phys. Chem. Chem. Phys. 17 (2015) 18924–18936.
[38] T. Cheng, H. Xiao, W.A. Goddard III, J. Am. Chem. Soc. 138 (2016) 13802–13805.
[39] S. Sen, D. Liu, G.T.R. Palmore, ACS Catal. 4 (2014) 3091–3095.
[40] K.J.P. Schouten, E.P. Gallent, M.T. Koper, J. Electroanal. Chem. 716 (2014) 53–57.
[41] T. Cheng, H. Xiao, W.A. Goddard, Proc. Natl. Acad. Sci. (2017) 201612106.
[42] H. Xiao, T. Cheng, W.A. Goddard III, R. Sundararaman, J. Am. Chem. Soc. 138 (2016) 483–486.
[43] X. Nie, M.R. Esopi, M.J. Janik, A. Asthagiri, Angew. Chem. Int. Ed. 52 (2013) 2459–2462.
[44] H. Xiao, T. Cheng, W.A. Goddard III, J. Am. Chem. Soc. 139 (2016) 130–136.
[45] R. Kortlever, J. Shen, K.J.P. Schouten, F. Calle-Vallejo, M.T. Koper, J. Phys. Chem. Lett. 6 (2015) 4073–4082.